PHYSICAL REVIEW B **95**, 174101 (2017)

Phase-field study of ripening and rearrangement of precipitates under chemomechanical coupling

C. Schwarze,[1] A. Gupta,[2] T. Hickel,[2] and R. Darvishi Kamachali[1,*]
[1]*Interdisciplinary Centre for Advanced Materials Simulation (ICAMS), Ruhr-University Bochum, 44780 Bochum, Germany*
[2]*Max-Planck-Institut für Eisenforschung GmbH, 40237 Düsseldorf, Germany*

(Received 8 January 2017; revised manuscript received 29 March 2017; published 9 May 2017; publisher error corrected 30 May 2017)

We investigate the evolution of large number of δ' coherent precipitates from a supersaturated Al-8 at.% Li alloy using large-scale phase-field simulations. A chemomechanical cross-coupling between mechanical relaxation and diffusion is taken into account by considering the dependence of elastic constants of the matrix phase onto the local concentration of solute atoms. The elastic constants as a function of solute concentration have been obtained using density functional theory calculations. As a result of the coupling, inverse ripening has been observed where the smaller precipitates grow at the expense of the larger ones. This is due to size-dependent concentration gradients existing around the precipitates. At the same time, precipitates rearrange themselves as a consequence of minimization of the total elastic energy of the system. It is found that the anisotropy of the chemomechanical coupling leads to the formation of new patterns of elasticity in the matrix thereby resulting in new alignments of the precipitates.

DOI: 10.1103/PhysRevB.95.174101

I. INTRODUCTION

Precipitation-hardened alloys have been successful candidates for many advanced industrial applications [1–9]. In particular, Al alloys are widely used in aerospace and automotive applications owing to their low density and high strength [10–15]. In these alloys, the interaction between precipitates and dislocations is known as the most important strengthening mechanism that strongly depends on the size and spacing between the precipitates [16–19]. The size and distance between the precipitates, however, vary during ageing and under service conditions. In particular, the elastic interaction due to misfit strains often accompany the precipitation process and has a great influence on the growth, shape and arrangement of the precipitates. Conventional Lifshitz, Slyozov, and Wagner (LSW) theory of ripening [20,21] investigates the evolution of precipitates from a supersaturated matrix in the presence of chemical driving forces. The influence of elastic interactions has been gradually introduced to this picture in seminal works of J. W. Cahn, A. G. Khachaturyan and others. For a detailed review see Fratzl *et al.* [22].

In addition to their individual effects on the precipitation, strain/stress and concentration gradients around the precipitates greatly overlap and may mutually influence each other during the nucleation, growth and ripening. This bilateral interaction between chemical/diffusional and mechanical aspects of the microstructure evolution is termed "chemomechanical" coupling in this study and expresses the interdependence between the mechanical properties and local composition of the material. The stress-driven fluxes resulting from the size mismatch of solute and solvent atoms (Vegard's law) have been widely investigated [23–26]. Another possibility of chemomechanical interaction arises when the elastic constants of a material depend on its composition. This aspect is important in alloys in which the bonds between solute and solvent atoms possess different strengths. If the elastic constants are assumed to be composition-dependent (locally), the mechanical response of the material is expected to be also composition-dependent. In turn, the composition of a material might change in the presence of internal stresses such as those generated by precipitates. For a single precipitate in an infinite matrix, Steinbach and coworkers [27] has shown that this effect leads to a strained equilibrium. Darvishi Kamachali *et al.* [28] have applied this concept of chemomechanical coupling to explain Ni depletion around a single Ni_4Ti_3 precipitate in NiTi shape memory alloys.

Recently, two of the current authors have extended the theory of chemomechanical coupling to the growth and ripening stage [29] by investigating the dynamic interaction between a pair of precipitates. A mechanism of inverse ripening has been discovered in which the smaller precipitate grows at the expense of the larger one. In addition, it is found that coherent precipitates might rearrange into new patterns when the concentration and strain/stress fields mutually evolve under the chemomechanical coupling. In the current study, we will examine these theories of inverse ripening and the rearrangement for a large number of randomly distributed precipitates evolving from a supersaturated matrix. Large-scale phase-field simulations and temporal analysis of size and position of the precipitates as well as temporal evolution of concentration field in the system are conducted. We study the formation of δ' (Al_3Li) precipitates in the Al-Li system. The accurate composition-dependence of the elastic constants of Al-Li matrix solid solution has been obtained using density functional theory (DFT) calculations. These results are directly used as input in the phase-field simulations. In Sec. II, the phase-field and DFT methodology and the theory of chemomechanical coupling are described. The setup and procedure of simulations and their analysis are presented in Sec. III. In Sec. IV, we evaluate our results. The size and distribution of the precipitates for different simulation setups with and without chemomechanical coupling are investigated. We remark on the effect of coherency loss on inverse ripening. Based on our findings experimental evaluations are proposed.

---

[*] Corresponding author: Reza Darvishi Kamachali, reza.darvishi@rub.de

II. THEORY AND MODELING

In this study, a multi-phase-field approach is employed for investigation of large number of precipitates. We solve the interface kinetics considering interface curvature, diffusion of solute atoms, and elasticity. For the sake of a systematic study, each of these features is deliberately turned on and off. In this section, we briefly describe the multi-phase-field and DFT method used in this study and review the recently proposed [29] theory of chemomechanical coupling and inverse ripening.

A. Phase-field modelling

The multi-phase-field concept [30,31] has shown its extensive applicability in studying microstructure evolution and phase transformations. Grain growth [32,33], nanograin growth [34], particle pinning [35], texture evolution and recrystallization [36], and precipitation [28,37] are examples of efficient application of multi-phase-field method in materials science. In this approach, the temporal evolution of individual nonconserved fields $\{\phi_\alpha\}$ is given by a generalized Ginzburg-Landau relation

$$\dot{\phi}_\alpha = -\frac{\mu}{N}\sum_{\beta=1}^{N}\left(\frac{\delta F}{\delta\phi_\alpha} - \frac{\delta F}{\delta\phi_\beta}\right), \tag{1}$$

where the indices α and β correspond to the domains of interest (precipitates and matrix phase, respectively), μ is interface mobility, and N is the number of domains. The antisymmetric nature of this relation imposes the constraint $\sum_{\alpha=1}^{N}\dot{\phi}_\alpha = 0$ in each point of space. Defining $\phi_\alpha \in [0,1]$, analogous to phase fractions, leads to the constraint $\sum_{\alpha=1}^{N}\phi_\alpha = 1$ on the phase fields. The free energy functional is given over the domain Ω:

$$F = \int_\Omega (f^{\mathrm{Intf}} + f^{\mathrm{Chem}} + f^{\mathrm{Elast}})\, dV, \tag{2}$$

where f^{Intf}, f^{Chem}, and f^{Elast} are the interface, chemical, and elastic free energy densities, respectively. The interface energies $\sigma_{\alpha\beta}$ are normalized by phase fields such that

$$f^{\mathrm{Intf}} = \sum_{\alpha=1\neq\beta}^{N}\sum_{\beta>\alpha}^{N}\frac{8\sigma_{\alpha\beta}}{\eta}\left(-\frac{\eta^2}{\pi^2}\nabla\phi_\alpha\cdot\nabla\phi_\beta + \phi_\alpha\phi_\beta\right), \tag{3}$$

with η being the width of the diffuse interface. The chemical and elastic free energy densities are weighted linearly with the respective phase fractions

$$f^{\mathrm{Chem}} = \sum_{\alpha=1}^{N}\phi_\alpha f_\alpha(c_\alpha) + \lambda\left[c - \sum_{\alpha=1}^{N}(\phi_\alpha c_\alpha)\right] \tag{4}$$

and

$$f^{\mathrm{Elast}} = \frac{1}{2}\sum_{\alpha=1}^{N}\phi_\alpha\left[\epsilon_\alpha^{\mathrm{ij}} - \epsilon_\alpha^{*\mathrm{ij}}\right]C_\alpha^{\mathrm{ijkl}}\left[\epsilon_\alpha^{\mathrm{kl}} - \epsilon_\alpha^{*\mathrm{kl}}\right], \tag{5}$$

where λ is the Lagrange multiplier for conservation of the solute concentration, $c = \sum_{\alpha=1}^{N}(\phi_\alpha c_\alpha)$ is the concentration of solute atoms, c_α are phase concentrations, ϵ^{ij} is total strain, $\epsilon^{*\mathrm{ij}}$ is eigenstrain, and C^{ijkl} are elastic constants. Inserting Eqs. (2)–(5) into Eq. (1) yields

$$\dot{\phi}_\alpha = \frac{\mu}{N}\sum_{\beta=1\neq\alpha}^{N}\left[\sum_{\gamma=1\neq\beta}^{N}(\sigma_{\beta\gamma} - \sigma_{\alpha\gamma})\left(\nabla^2\phi_\gamma + \frac{\pi^2}{\eta^2}\phi_\gamma\right) + h(\{\phi_\alpha\})\left(\Delta G_{\alpha\beta}^{\mathrm{Chem}} + \Delta G_{\alpha\beta}^{\mathrm{Elast}}\right)\right] \tag{6}$$

in which $h(\{\phi_\alpha\})$ is a weighting function and $\Delta G_{\alpha\beta}^{\mathrm{i}}$ are the driving forces between pairs of phase fields. For a dual interface, one can show that the phase-field model reproduces the Gibbs-Thompson kinetic equation

$$\frac{V}{\mu} = \sigma K + \Delta G^{\mathrm{Chem}} + \Delta G^{\mathrm{Elast}} \tag{7}$$

in 1D and for spherical symmetries with σ being the isotropic interface energy, $V = \dot{\phi}\phi_x^{-1}$ and $h(\phi) = \phi_x$ [38], assuming the driving forces (ΔG^{i}) are constant. The concentration of solute atoms is obtained from the continuity equation

$$\dot{c} + \nabla\cdot\left(M\nabla\frac{\delta F}{\delta c}\right) = 0, \tag{8}$$

where M is the atomic mobility. Instantaneous mechanical equilibrium is achieved by solving the force balance:

$$\nabla\frac{\delta F}{\delta\epsilon^{\mathrm{ij}}} = \vec{0}. \tag{9}$$

B. Modeling and theory of chemomechanical coupling

The idea of coupling is developed based on the fact that in a solid solution the strength of atomic bonds can vary locally by adding solute atoms. Although this has been pointed out long ago [25,39], composition-dependency of stiffness matrix was largely neglected until recently when we have studied its influence on the precipitation [27–29]. Similar to these works, a linear relation between the elastic constants of the matrix phase and the solute concentration is assumed

$$C^{\mathrm{ijkl}}(c) = C_0^{\mathrm{ijkl}}(1 + \kappa^{\mathrm{ijkl}}\,\Delta c), \tag{10}$$

where C_0^{ijkl} are the reference elastic constants of the matrix parent phase at $c = c_{\mathrm{ref}}$ (c_{ref} is the composition of reference matrix phase), $\kappa = \kappa^{\mathrm{ijkl}}$ is a coupling factor having the same symmetry and components as C_0^{ijkl} and $\Delta c = c(x,t) - c_{\mathrm{ref}}$. This relation couples the mechanical equilibrium [Eq. (9)] to the local composition. In turn, the diffusional flux $\vec{J}$ of solute atoms couples back to the elastic energy as

$$\vec{J} = -D\nabla c - M\nabla\frac{\partial f^{\mathrm{Elast}}}{\partial c} \tag{11}$$

in which $D = M\mathcal{R}T$ is the diffusion coefficient with $\mathcal{R}$ being the gas constant. The first term on the right-hand side is the classical Fick's law and the second term describes fluxes under the gradients of elastic energy which exist around the self-stress sources, i.e., the precipitates. Thus diffusion results in a reduction of total elastic energy. This in enabled via local softening/stiffening of the matrix since the elastic constants of the matrix phase are composition-dependent

[Eq. (10)]. Furthermore, the second term leads to a nontrivial concentration profile around a precipitate which controls its evolution and interaction with the neighboring precipitates. For an isotropic precipitate of radius R with volumetric expansion, the quasi-steady-state solution for the concentration profile has been given by [29]

$$c(r) = c_0 - g_0\kappa\left(\frac{R}{r}\right)^6 + (g_0\kappa - g_1)\frac{R}{r} + O(\kappa^2) \tag{12}$$

in which $g_0 = \frac{6G_m V_m b^2}{\mathcal{R}T}$ and $g_1 = c_0 - c_R = \Delta - \frac{l}{R}$ with Δ and $l = \frac{2\sigma V_p c_\infty}{\mathcal{R}T}$ being the supersaturation and capillarity length, respectively. Here, G_m is the shear modulus of the matrix, V_m is the molar volume of the matrix, c_0 is the matrix composition far from the precipitate, c_R is the equilibrium composition at the surface of the precipitate, and b is a materials constant (see Ref. [29] for details). Equation (12) expresses mechanically modified concentration field around a precipitate when the elastic constants of the matrix depend on the solute concentration. The additional terms, $-g_0\kappa(\frac{R}{r})^6 + g_0\kappa\frac{R}{r}$, cause strained concentration gradients[1] introduced in the presence of chemomechanical coupling ($\kappa \neq 0$). Note that g_0 is a positive coefficient independent of the sign of eigenstrain ϵ^*_p. These terms are indeed responsible for the additional (mechanically driven) flux of solute atoms. It has been shown [29] that for certain thermo-elasto-physical properties of the system, $5g_0\kappa + \Delta > \frac{l}{R}$, the inverse ripening becomes possible in which smaller precipitates grow at the expense of larger precipitates. In this study, we examine this theory of inverse ripening for a large number of randomly distributed precipitates. Here the terms "chemomechanical coupling," "crosscoupling," and "coupling" relates to solving Eqs. (8) and (9), simultaneously, using (10) and (11). We investigate precipitate ripening with ($\kappa \neq 0$) and without ($\kappa = 0$) coupling effect to specify its effect on the ripening and rearrangement of the precipitates.

C. Homogenization of mechanical properties and driving forces

Across the diffuse interface ($\phi_\alpha \neq 0$), the mechanical properties in the two-phase region are homogenized. Since these mechanical properties are influenced by the chemomechanical coupling (Sec. II B), a reevaluation of the homogenization scheme is necessary as follows. We have employed Reuss scheme which assumes a constant stress, $\bar{\sigma} = \bar{\sigma}_\alpha = \bar{\sigma}_\beta$, across the phases. The sum of individual strains $\epsilon^{\text{total}} = \epsilon^{\text{el}} + \epsilon^*$ is given by (we omit the spatial indices for the sake of readability)

$$\epsilon^{\text{total}} = \sum_{\alpha=1}^{N} \phi_\alpha \epsilon^{\text{total}}_\alpha. \tag{13}$$

The effective eigenstrain and compliance (across the diffuse interface) follow

$$\epsilon^* = \sum_{\alpha=1}^{N} \phi_\alpha \epsilon^*_\alpha \tag{14}$$

and using Eq. (10)

$$S_{\text{eff}} = \sum_{\alpha=1}^{N} \phi_\alpha (C_{0,\alpha}(1 + \kappa_\alpha \Delta c))^{-1}. \tag{15}$$

Thus the elastic strain and stress can be obtained as

$$\epsilon^{\text{el}} = \sum_{\alpha=1}^{N} \phi_\alpha\ \bar{\sigma}\ S_\alpha(c) \tag{16}$$

and with $C_{\text{eff}} = S^{-1}_{\text{eff}}$

$$\begin{aligned}\bar{\sigma} &= C_{\text{eff}}(\epsilon^{\text{total}} - \epsilon^*)\\ &= \left[\sum_{\alpha=1}^{N} \phi_\alpha (C_\alpha(1 + \kappa_\alpha \Delta c))^{-1}\right]^{-1} \left(\epsilon^{\text{total}} - \sum_{\alpha=1}^{N} \phi_\alpha \epsilon^*_\alpha\right).\end{aligned} \tag{17}$$

Note that the compliances also carry the composition-dependency similar to the elastic constants as described in Sec. II B. The total elastic energy density is

$$\begin{aligned}f^{\text{Elast}} &= \sum_{\alpha=1}^{N} \phi_\alpha f^{\text{Elast}}_\alpha\\ &= \frac{1}{2}\left(\sum_{\alpha=1}^{N} \phi_\alpha (\epsilon^{\text{total}} - \epsilon^*) C_{\text{eff}} (\epsilon^{\text{total}} - \epsilon^*)\right)\end{aligned} \tag{18}$$

and the elastic driving force will be

$$\begin{aligned}\Delta G^{\text{Elast}}_{\alpha\beta} &= -\left(\frac{\partial}{\partial\phi_\alpha} - \frac{\partial}{\partial\phi_\beta}\right) f^{\text{el}}\\ &= \bar{\sigma}\Big[(\epsilon^*_\alpha - \epsilon^*_\beta) + \frac{1}{2}(S_\alpha - S_\beta)\\ &\qquad \times (\epsilon^{\text{total}} - \epsilon^*) C_{\text{eff}} (\epsilon^{\text{total}} - \epsilon^*)\Big].\end{aligned} \tag{19}$$

The chemical driving force reads

$$\Delta G^{\text{Chem}}_{\alpha\beta} = m \Delta S_0 (c - c_{\text{eq}}) \tag{20}$$

with m the slope between matrix single and two-phase region in the T-c diagram, $\Delta S_0 = -9.7315 \times 10^5\ \text{J}\,\text{K}^{-1}\,\text{m}^{-3}$ [40] the experimentally determined entropy of formation of the ordered δ' where the reference states of fcc Al and bcc Li were used [41], and $c_{\text{eq}} = 6.67$ at.% the equilibrium matrix concentration (at a flat interface) at the annealing temperature of 473.15 K (200 °C). Equations (18) and (20) enter the temporal equation of phase fields [Eq. (6)]. The chemomechanical potential in Eq. (11) is obtained as

$$\frac{\partial f^{\text{Elast}}}{\partial c} = \frac{1}{2}\sum_{\alpha=1}^{N} (\epsilon^{\text{total}} - \epsilon^*) \frac{\partial S^{-1}_{\text{eff}}}{\partial c} (\epsilon^{\text{total}} - \epsilon^*) \tag{21}$$

---

[1] In this context, the term "strained concentration gradients" is used to express dynamic concentration profile enforced by mechanically-driven fluxes around the precipitate that evolves as the precipitate evolves. This is different from the statically strained profiles described in our earlier work [27].

with

$$\frac{\partial S_{\text{eff}}^{-1}}{\partial c} = -S_{\text{eff}}^{-1}\left[\sum_{\alpha=1}^{N}\left(\phi_\alpha C_\alpha^{-1}(c)(-C_{0,\alpha}\kappa_\alpha)C_\alpha^{-1}(c)\right)\right]C_{\text{eff}} \tag{22}$$

and $C_\alpha(c) = C_{0,\alpha}(1+\kappa_\alpha \Delta c)$.

D. Formalism of elastic constants calculations

Ab initio calculations are conducted in order to determine the dependence of elastic constants on the solute concentrations of the matrix phase. The Al-rich Al-Li alloy has face-centred cubic (fcc) crystal structure. Therefore the evaluation of their complete elasticity/stiffness matrix characterized otherwise by 21 independent components is reduced to the determination of only three elastic constants namely C_{11}, C_{12}, and C_{44} (since $C_{11} = C_{22} = C_{33}$, $C_{12} = C_{23} = C_{31}$, and $C_{44} = C_{55} = C_{66}$ for cubic symmetry) [42]. Here, we have used the Voigt notation to express the fourth-order tensor components C^{ijkl} [introduced in Eq. (10)] in a reduced form as the components of second-order tensor where $C_{11} = C^{1111}$, $C_{12} = C^{1122}$, and $C_{44} = C^{2323}$. Within the framework of first-principles based total energy calculations, these elastic constants are obtained by applying a strain tensor ϵ to the crystal lattice thereby resulting in a lattice distortion $\mathbf{r}' = (I+\epsilon)\mathbf{r}$, where $\mathbf{r}$ and $\mathbf{r}'$ are the lattice vectors before and after the distortion and I is the unit matrix. The matrix components C_{11}, C_{12}, and C_{44} are calculated by applying volume conserving orthorhombic ϵ_{ortho} and monoclinic ϵ_{mono} strains (characterized by a distortion δ) to the lattice defined as [43]

$$\epsilon_{\text{ortho}} = \begin{pmatrix} \delta & 0 & 0 \\ 0 & -\delta & 0 \\ 0 & 0 & \delta^2/(1-\delta^2) \end{pmatrix} \quad \text{and}$$

$$\epsilon_{\text{mono}} = \begin{pmatrix} 0 & \delta/2 & 0 \\ \delta/2 & 0 & 0 \\ 0 & 0 & \delta^2/(4-\delta^2) \end{pmatrix}. \tag{23}$$

The energies $E(\delta)$ of the crystal structures subjected to the above defined strains are then Taylor expanded around the equilibrium position ($E(\delta = 0)$) for small deformations and expressed in terms of δ as

$$E_{\text{ortho}}(\delta) = E(0) + C' V_{\text{eq}}\delta^2 + O[\delta^4] + \dots, \tag{24}$$

$$E_{\text{mono}}(\delta) = E(0) + \tfrac{1}{2} C_{44} V_{\text{eq}}\delta^2 + O[\delta^4] + \dots, \tag{25}$$

where V_{eq} is the equilibrium volume and $C' = C_{11} - C_{12}$ is the shear modulus. Ignoring the higher order terms in δ ($O[\delta^4]$ and further), we calculate the strain energy density U as $U(\delta) = [(E(\delta) - E(0))/V_{\text{eq}}]$. Finally, taking its second derivative with respect to δ we get $\frac{\partial^2 U_{\text{ortho}}}{\partial \delta^2} = 2(C_{11} - C_{12})$ and $\frac{\partial^2 U_{\text{mono}}}{\partial \delta^2} = C_{44}$. For cubic crystals, C_{11} and C_{12} are evaluated using their above relation to U_{ortho} in conjunction with their relation to the bulk modulus $B_M = \frac{1}{3}(C_{11} + 2C_{12})$, where B_M is calculated by performing a least-squares fit to the energy-volume curve as per the Murnaghan equation of state [44].

TABLE I. Elastic constants for pure Al matrix (obtained by DFT calculations) and δ' phase [49,50].

Phase	C_{11} [GPa]	C_{12} [GPa]	C_{44} [GPa]
Matrix phase	107.1	62.9	28.9
Al_3Li	139.8	33.7	40.7

III. SIMULATION PROCEDURE

A. Setup of phase-field simulations

The phase-field simulations including the chemomechanical coupling are performed using the OpenPhase software [45]. The simulation box with 256^3 grid cells and a grid size $\Delta x = 1$ nm is chosen with periodic boundary conditions and a time stepping $\Delta t = 0.25$ s. A supersaturated Al-8 at.% Li alloy is considered where coherent δ' precipitates form at 473.15 K (200 °C). The diffusion coefficient at this temperature is 1.2×10^{-18} m^2 s^{-1} [46] and the interface energy is 0.014 J m^{-2} [47]. The δ' precipitates are assumed to be stoichiometric (Al_3Li) without internal diffusion and therefore without chemomechanical coupling effect. Both phases have cubic crystals with elastic constants listed in Table I. The transformation strain of precipitates is −0.1% [48].

The objective of our simulations lies in studying the evolution of large number of precipitates during ripening including the aspects of chemomechanical coupling described in Sec. II B. Under the conditions of this coupling, we explore the possibility for inverse ripening and rearrangement of the precipitates as predicted in Ref. [29]. There are two thermodynamic phases in the simulation box. Five-hundred precipitate nuclei with a single-grid size are randomly planted in the matrix phase [including the matrix phase, $N = 501$ in Eq. (1)]. The same nucleation sites are considered for all the simulations. The investigations are conducted in a systematic manner (i) without elasticity (pure curvature and chemical evolution), (ii) with elasticity but no coupling, and (iii) with elasticity and coupling. In this way, we aim to capture the specific influence of chemomechanical coupling and compare its effect against other contributions during ripening. Two different cases of coupling are considered: We use anisotropic coupling factors (a.i.) obtained by DFT calculations (Sec. IV A) and compare the outcome against the isotropic coupling ($\kappa = 0.01$ at.%$^{-1}$). The coupling values are listed in Table II.

B. Setup of DFT calculations

The elastic constants were obtained by taking the derivatives of the strain energy densities with respect to the applied deformation. For this purpose, the total energies required to evaluate expressions (24) and (25) and the bulk modulus

TABLE II. The coupling factors κ (10). The anisotropic (a.i.) values are obtained by DFT calculations (Sec. IV A). The isotropic values are used for comparison.

System	κ_{11} [at.%$^{-1}$]	κ_{12} [at.%$^{-1}$]	κ_{44} [at.%$^{-1}$]
Isotropic	0.01	0.01	0.01
Anisotropic	0.0052	−0.0231	0.0457

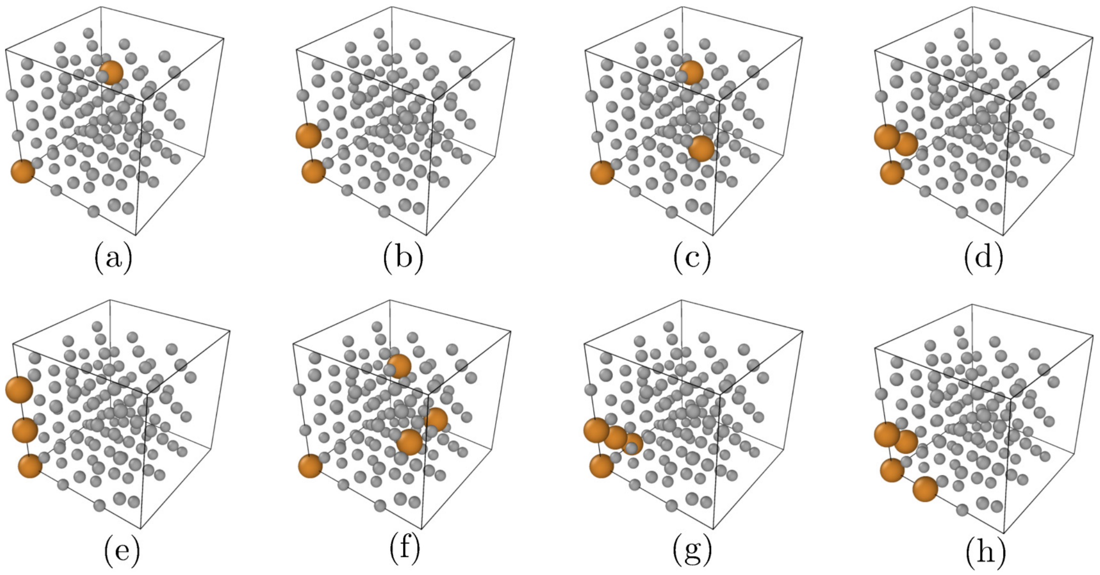

FIG. 1. (Supercell configurations ($Al_M Li_N$ for $N > 1$) considered in the present work for the total energy calculations within the DFT framework. (a) and (b) $Al_{106}Li_2$, (c)–(e) $Al_{105}Li_3$, and (f)–(h) $Al_{104}Li_4$. The gray and golden spheres represent the Al and Li atoms, respectively. The golden spheres are enlarged for the sake of highlighting the solute atoms.

have been calculated employing the projector augmented wave (PAW) method as implemented in the VASP [51,52] package with energetics based on density functional theory (DFT). The generalized gradient approximation (GGA) within the Perdew-Burke-Ernzerhof (PBE) parametrization scheme [53] was opted to describe the electronic exchange and correlation effects. S/PHI/NX [54] package was used to calculate the bulk modulus B_M from the Murnaghan equation of state [44]. All our energy calculations were performed using a $3 \times 3 \times 3$ fcc supercell (108 atoms) with an equilibrium lattice parameter value of 4.04 Å corresponding to pure Al. The integration over the Brillouin zone was performed using the Monkhorst-Pack [55] scheme with an $8 \times 8 \times 8$ reciprocal-space k-mesh centered around the Γ point and utilizing the Methfessel-Paxton scheme [56] with a thermal smearing width of 0.2 eV to account for the smoothening of partial occupancies of the electronic states. The plane-wave energy cutoff was set to 400 eV. An energy of 10^{-6} eV was used as a convergence criterion for the self-consistent electronic loop. The total energies were calculated for 17 equally spaced δ values ranging between $\pm 2\%$ (-0.02, -0.0175, -0.015, ..., 0.015, 0.0175, 0.02) and were fitted to Eqs. (24) and (25) considering only up to second order terms in the expansion. In all the calculations, volume-conserving strains were applied [43,50]. The internal atomic coordinates were fully relaxed during the total energy calculations maintaining a constant volume.

In order to determine the bulk modulus from the Murnaghan equation of state [44], a set of energies $\{E_i\}$ was calculated at 13 different equally spaced volumes $\{V_i\}$ around the equilibrium volume of pure fcc Al. All the elastic properties mentioned in Sec. II D have been calculated for a Li concentration ranging from 0–3.7 at. % in an otherwise pure fcc Al matrix. Within the framework of supercell based total energy calculations, this concentration range correspond to a substitutional solid solution represented by a 108 atom fcc-supercell $Al_{108-N}Li_N$ with $N = 0 \ldots 4$ solute atoms. For $N > 1$, we have considered 2–3 configurations (see Fig. 1) out of *several possible* configurations of solute atoms within the matrix. We performed the convergence tests for the elastic constants with respect to the plane-wave energy cutoff and the reciprocal-space k mesh varying from 250–500 eV and $2 \times 2 \times 2 - 14 \times 14 \times 14$ k points, respectively, for $Al_{107}Li_1$ supercell. For the settings used ($E_{\text{cut}} = 400$ eV and k mesh $= 8 \times 8 \times 8$), B_M, C_{11}, C_{12}, and C_{44} were found to be converged within less than 0.5, 3, 3, and 4 GPa, respectively. Owing to the anisotropic nature of the strain matrices ϵ_{ortho} and ϵ_{mono} [Eq. (23)], we arithmetically average over three different strain matrices by interchanging the direction of applied deformations among the x, y, and z axes. This is done in order to include the effect of configurational asymmetry and the directional dependence of solute-solute interactions posed by a given solute configuration in an averaged manner. For a single solute atom ($N = 1$) within a matrix, the elastic constants will be invariant to the direction of the applied strain.

C. Methods of analysing simulation results

The evolution of each precipitate is analysed based on its volume and center of mass extracted during the simulations. From these data, several properties of the system are calculated. The radius of each precipitate R_i is obtained by defining an equivalent sphere volume V_i:

$$R_i = \sqrt[3]{\frac{3V_i}{4\pi}}. \tag{26}$$

This is a good approximation as δ' precipitates are almost spherical. The average radius $\langle R \rangle$ is obtained by

$$\langle R \rangle = \frac{1}{n_{\text{ex}}(t)} \sum_{i=1}^{n_{\text{ex}}(t)} R_i, \tag{27}$$

with $n_{\rm ex}(t)$ the total number of existing precipitates at time t. In order to investigate the rearrangement of precipitates, we track the center of mass of precipitates $\mathrm{P}_n(\mathrm{x}_n|\mathrm{y}_n|\mathrm{z}_n)$. Averaging the total shift of all existing precipitates over simulation period t^*, we obtain

$$l(t) = \sum_{t=0}^{t^*} \frac{1}{n_{\rm ex}(t)} \sum_{n=1}^{n_{\rm ex}(t)} \sqrt{(x_{n,t} - x_{n,t-1})^2 + (y_{n,t} - y_{n,t-1})^2 + (z_{n,t} - z_{n,t-1})^2}. \tag{28}$$

Furthermore, the relative angular position of the neighboring precipitates for each single precipitate and with respect to crystallographic orientations in the fcc matrix are mapped over time. For each precipitate, we consider neighboring precipitates at $P_m(x_m|y_m|z_m)$ within a critical radius $r_{\rm crit} = 32\,\mathrm{nm}$—the ideal distance if 500 precipitates exists in a $256^3\ \mathrm{nm}^3$ box-size on a periodic pattern—and evaluate r, Θ, and Φ in spherical coordinates as

$$r = \sqrt{(x_m - x_n)^2 + (y_m - y_n)^2 + (z_m - z_n)^2}\quad , \tag{29}$$

$$\Theta = \arccos\left(\frac{y_m - y_n}{r}\right)\quad , \tag{30}$$

$$\Phi = \arctan\left(\frac{z_m - z_n}{x_m - x_n}\right) \tag{31}$$

for each neighboring precipitate. The temporal evolution of the angular coordinate reveals the relative arrangement of the precipitates over the course of ripening. Phase fields, concentration, strain, and stress fields are stored and used to draw 3D and 2D microstructural properties.

IV. RESULTS AND DISCUSSIONS

A. DFT Studies of composition-dependent elastic constants

For Al-Li, an almost linear decrease in B_M with an increasing Li concentration is observed [dashed line in Fig. 2(a)]. This is in line with previous observations [58–61] of decreasing B_M with increasing Li ($B_M^{\rm Al} > B_M^{\rm Al_3Li} > B_M^{\rm AlLi} > B_M^{\rm Al_2Li_3} > B_M^{\rm Al_4Li_9} > B_M^{\rm AlLi_3} > B_M^{\rm Li}$) owing to the rather low B_M value [62] of pure Li at around 12.1 GPa. The calculated B_M agrees both qualitatively and quantitatively well with the available experiments [57] since deviations of $\pm10\%$ are expected in DFT calculations. The existing difference of $\approx 2\%$ is also partially attributed to the fact that the measurements were performed at room temperature ($21\,^\circ\mathrm{C} = 294$ K), whereas our calculated values correspond to 0 K and the bulk modulus typically decreases with temperature.

We observe an almost linear increase in C_{11} [Fig. 2(b)] with Li concentration up to 3.7 at.%. C_{12}, however, exhibits a linear decrease with increase in Li concentration [Fig. 2(c)]. For both C_{11} and C_{12}, our results agree considerably better with the experiments [57] throughout the considered concentration range as compared to the previous calculations performed employing the elastic-muffin tin orbital (EMTO) approach [50]. The high negative slope of $C_{12}(c)$ [Fig. 2(c)] as compared to the low positive slope of $C_{11}(c)$ [Fig. 2(b)] consequently results in an overall reduction of the bulk modulus [Fig. 2(a)] of Al-Li alloy [$B_M = \frac{1}{3}(C_{11} + 2C_{12})$]. For C_{44} [Fig. 2(d)], we observe a linear increase with Li concentration agreeing well with the linear trend observed in experiments [57] and a much better accuracy as compared to the previous results obtained within the EMTO approach. The uncertainty intervals given in Fig. 2 represent the result of different configurations shown in Fig. 1, but the number of calculations is too low to consider them as statistical error bars. The results of DFT calculations justify the linear relation between elastic constants and Li concentration given in Eq. (10). The anisotropic set of coupling factors κ is extracted for $C^{\rm ij}$s and listed in Table II. This information is directly used in the phase-field simulations discussed below.

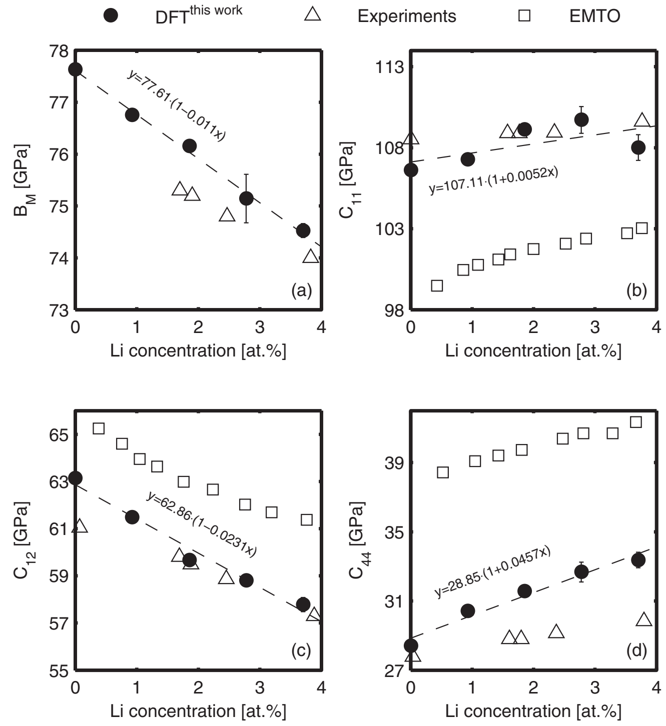

FIG. 2. Calculated and measured elastic constants for Al rich Al-Li alloys as a function of Li concentration (0–3.7 at.%). (a) Bulk modulus B_M, (b) C_{11}, (c) C_{12}, and (d) C_{44}. The filled circles present our results. The standard error is calculated as $\sigma_{\bar{x}} = \sigma/\sqrt{n}$, where σ is the standard deviation of the set of data points and n is the number of considered data points (different configurations) corresponding to a particular Li concentration. The dashed lines represents the linear fits the slope of which gives chemomechanical coupling factors κ. We compare our results vs experiments [57] (triangles) and previous calculations (squares) based on EMTO approach [50].

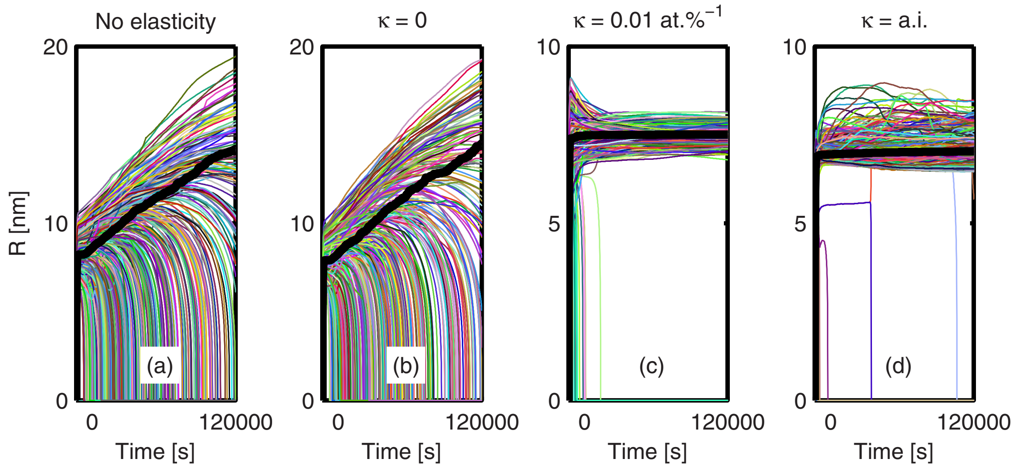

FIG. 3. Precipitates radii over time for different simulation settings and average precipitate radii (thick black lines).

B. Phase-field investigations

The phase separation is classically divided in two steps of (i) growth, during which all the precipitates exchange solute/solvent atoms with the matrix along an increase in their volume, and (ii) ripening, when the precipitates compete against each other and some of them shrink and eventually disappear. In this study, we are mainly interested in studying the ripening process and the effect of chemomechanical coupling as described in Sec. II B. Conventional ripening process is known to be dominated by the size difference amongst the precipitates but it might also be influenced by their local configuration, especially when precipitates interact elastically [63,64]. The chemomechanical coupling model, however, introduces more complex aspects of phase separation as presented in Ref. [29]. In Sec. IV B 1, we present and discuss our simulation results with respect to the kinetics of ripening in the presence of chemomechanical coupling. In Sec. IV B 2, we focus on the elastic interaction of the precipitates and the effect of composition-dependent elastic constants on the rearrangement of the precipitates.

1. Kinetics of inverse ripening

Figure 3 shows the size evolution of all precipitates [Eq. (26)] over time for different simulation settings. We conduct simulations (a) without elasticity, (b) without coupling, and with (c) isotropic, and (d) anisotropic chemomechanical coupling. The thick black line in each plot represents the average precipitate radius [Eq. (27)]. The microstructure evolves from randomly distributed nuclei, but the same nucleation sites in all simulations. In the following, we first discuss the simulation results without the consideration of chemomechanical coupling and then focus on the effect of coupling.

Figure 3(a) shows the evolution of precipitates in the absence of elastic effects. All precipitates grow within a short period of time at the beginning of the simulation. After the growth, conventional ripening is observed during which the larger precipitates grow at the expense of the smaller ones. This is consistent with the LSW theory of ripening where precipitates compete only with respect to their size. The additional consideration of elasticity (without chemomechanical coupling, i.e., $\kappa = 0$) shows a minor effect on the overall evolution [Fig. 3(b)]. Figure 4(a) compares the average radius of precipitates for different simulation setups. Without the chemomechanical coupling, the kinetics of ripening is found to be in a good agreement with the LSW theory [20,21] where the cubic average grain size scales linearly with time ($\langle R\rangle^3 = Kt$ + const.). We found that elasticity slightly suppresses the early growth stage but accelerates the ripening in the later stages. Nevertheless, conventional ripening is found to occur in the presence of elasticity.

Taking chemomechanical coupling into account changes the whole course of ripening: An abnormal ripening behavior is observed in which the smaller precipitates grow at the expense of the larger ones (inverse ripening). After initial growth, most of the smaller precipitates continue growing and equilibrate their size. Figures 3(c) and 3(d) show the simulation results in the presence of isotropic and anisotropic chemomechanical coupling, respectively (see Table II for coupling factors). The anisotropic coupling values are obtained using DFT calculations as described in Sec. IV A. Whilst for isotropic coupling [Fig. 3(c)] most of the precipitates converge to a fine range of size, the anisotropic coupling [Fig. 3(d)] results in a much more complex evolution of precipitates in which the precipitates radii rise and fall over the course of inverse ripening. There

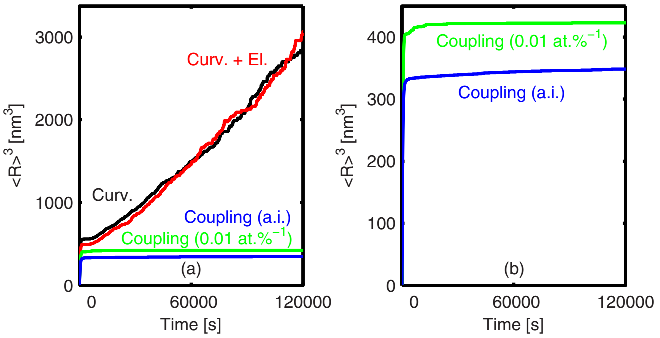

FIG. 4. (a) Average precipitate radii over time for different simulation settings and (b) magnified for mechanically coupled systems ($\kappa \neq 0$).

TABLE III. Growth coefficient K for different simulations. These are obtained by fitting to $\langle R\rangle^3 = Kt$ + const. in the later stages of ripening. a.i. are anisotropic coupling values obtained by DFT calculations.

Coupling value κ (at.%$^{-1}$)	Growth coefficient K (nm^3 s^{-1})
0	0.012
0.01	0.0004
a.i.	0.0024

is still a small net ripening that occurs as shown in Figs. 4(a) and 4(b). This is because of coalescence of some precipitates which are sitting closer to each other than a critical distance. This, however, occurs rarely in the simulations as the density of precipitates is relatively low. The growth coefficient K is listed in Table III for all simulations. The value of K for anisotropic coupling (0.0024) is six times higher than that for isotropic coupling (0.0004) whilst without the coupling $K = 0.012$.

The 3D microstructure of different simulation boxes as well as the concentration and pressure maps after 120000 s are compared in Fig. 5. The precipitate densities for systems with chemomechanical coupling (mid and bottom left figures) are much higher than those observed in the absence of coupling (top left). For $\kappa \neq 0$, most of the precipitates undergo inverse ripening and equilibrate their size. The results of our simulations confirm the theoretical works on chemomechanical coupling for pair precipitates [29]. The inverse ripening is a result of long-range coupling effect that dictates depletion of solute atoms in the vicinity of the precipitates. The mechanically driven fluxes around the precipitates [Eq. (11)] push indeed the solute atoms back into the matrix. This is reflected in the steady state in Eq. (12) where additional terms appear due to the coupling. Mechanically driven fluxes rapidly develop around the precipitates at the early stages of growth and evolve as the precipitate evolves. Figure 6 shows the temporal evolution of the concentration from growth (500 s) to ripening ($\geqslant$1000 s). While the number of precipitates decreases during normal ripening ($\kappa = 0$), the precipitate number is almost constant for inverse ripening. For different coupling

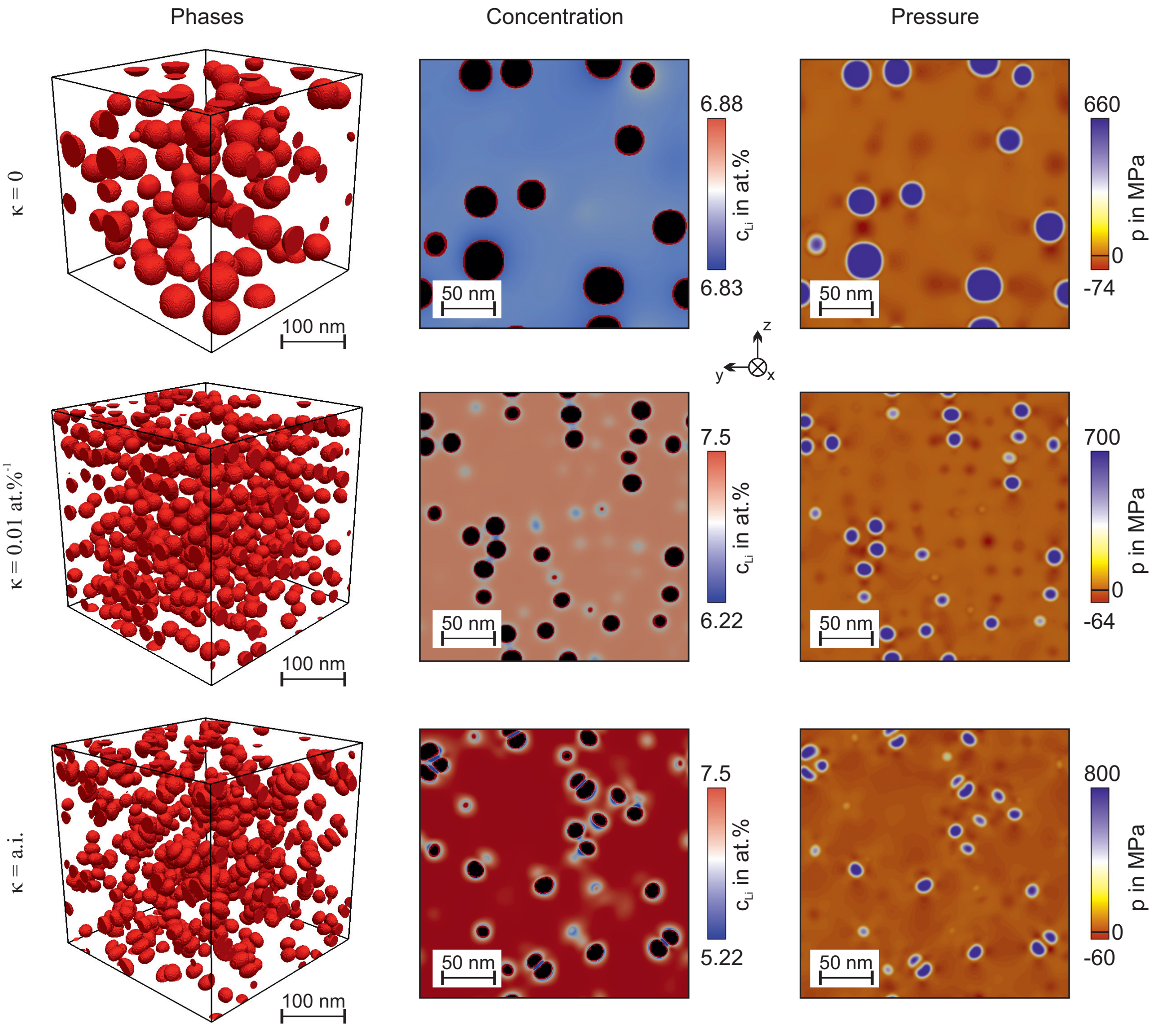

FIG. 5. 3D microstructures (left), 2d concentration (center) and pressure (right) plots (y-z plane at $x = 128$ nm) for different simulations ($\kappa = 0$, 0.01 at.%$^{-1}$, and a.i.) after 120 000 s. Li concentration in the precipitates (black colored) is 25 at.%. Note that the chemomechanical coupling influences the range of concentration and pressure in each system.

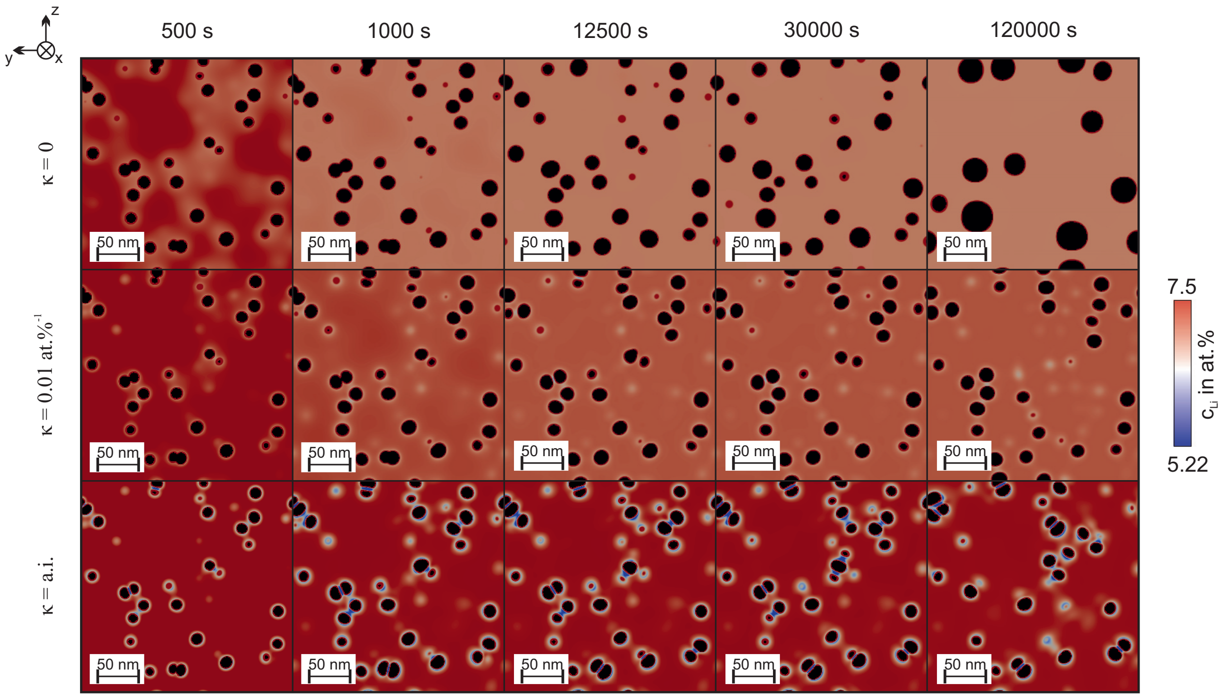

FIG. 6. Temporal evolution of concentration (y-z plane at $x = 128$ nm) for different simulations ($\kappa = 0$, 0.01 at.$\%^{-1}$, and a.i.). Li concentration in the precipitates (black colored) is 25 at.%.

factors, the change in the matrix concentrations due to the chemomechanical coupling [29] can be observed. Also solute depletion next to the precipitates and its evolution during the precipitation are visible in Figs. 5 and 6. This is in contrast to the conventional ripening where the solute is depleted around growing (larger) precipitates and enriched around shrinking (smaller) precipitates as compared in Fig. 6. In the presence of chemomechanical coupling, the supersaturation felt by the precipitates is approximately $5g_0\kappa + \Delta$ that depends on the coupling value κ. This also influences the range of concentration and stress/strain fields in the simulations (see also Figs. 1 and 3 in Ref. [29]). The competing condition for ripening is, therefore, modified in the presence of chemomechanical coupling ($\kappa \neq 0$). For $5g_0\kappa + \Delta > \frac{l}{R}$, the new supersaturation overcomes the interface capillarity effect and inverse ripening becomes possible [29]. Thus, for a certain combination of thermo-chemo-mechanical properties, small precipitates have a steeper profile compared to large precipitates which inverts the flux from large precipitates to small precipitates until they equilibrate. In particular, the capillarity effect depends on the precipitate/matrix interface energy. If the interfacial energy is large, smaller precipitates become energetically unfavourable and inverse ripening does not occur. It is to note that the chemomechanical coupling does not influence the equilibrium composition at the interface, unlike the elastic energy itself that has an energetic Gibbs-Thompson-like effect on the equilibrium concentration. On the other hand, the composition or size dependence of the interface energy and interface composition do not affect Eq. (12) but they are only boundary values for this solution. However, if the interface energy increases during the ripening by any mechanism, including being composition- or size-dependent, the inverse ripening can be eventually overcome once the capillarity effect dominates. In our setup, conventional ripening has been recovered for an interface energy as large as $\sigma \geqslant 0.14$ J m^{-2} (not shown here). Furthermore, the sign of the coupling factor influences the direction of composition fluxes. While a positive coupling ($\kappa > 0$) leads to solute depletion around the precipitate, a negative coupling ($\kappa < 0$) leads to solute enrichment and thus inverse ripening does not occur.

Wang *et al.* [63,64] have shown that precipitates may undergo inverse ripening due to their relative positioning in the presence of an elastic interaction. Su and Voorhees [65] have shown the possibility of inverse ripening depending on the morphology and size of the precipitates but a stabilization against ripening has not been observed for a many-particle system. Johnson and coworkers [66,67] also proposed a mechanism of inverse ripening due to elastic interaction between a pair of precipitates. This mechanism, however, is based on the modifications to the interface concentration due to elasticity. The current mechanism of inverse ripening has its origin in the far-field composition correction by the chemomechanical coupling while, as mentioned before, it does not influence the interface composition, i.e., $c(r = R) = c_R$. Furthermore, Nishimori and Onuki have reported slow decomposition kinetics when modulus inhomogeneity was introduced by composition-dependent elastic constants [68] and shear moduli [69] of the two phases. Their 2D simulations, however, are difficult to be compared to our 3D results. Several experimental studies on the coarsening behavior of δ' precipitates [70–72] reported conventional ripening but a sluggish increase in the maximum precipitate size [72]. The elastic interaction due to the formation of δ' precipitates, however, were neglected in these works. In Sec. IV C, we address the challenges in observing inverse ripening in the experiments.

2. Rearrangement of precipitates

The strained concentration gradients due to composition-dependent elastic constants [Eqs. (10) and (12)] naturally result in a heterogeneous matrix in terms of composition and elasticity. For an anisotropic coupling, the degree and symmetries of elastic anisotropy of the matrix are also subject to change. Theoretical study of chemomechanical coupling [29] proposes that elastic response of the matrix phase and arrangement of the precipitates will be greatly influenced by chemomechanical coupling. Using large-scale simulations we are able to examine this idea in a realistic setup where large number of precipitates interact with each other. In order to understand the effect of elastic interaction and rearrangements of the precipitates, we have evaluated the motion of precipitates during the growth and ripening as described in Sec. III C.

Figure 7(a) shows the average distance traveled by the precipitates with respect to their initial position as a function of time [Eq. (28)]. In principle, the precipitates "migrate" to minimize the overall energy of the system. This occurs via diffusion-controlled dissolution/growth phenomena. Both conventional ripening and elastic interaction between the precipitates may result in this motion. The former is because of the asymmetry of growth/shrinkage that depends on the local neighbourhood of the precipitates and the latter is driven by a decrease in the total elastic energy. Both mechanisms, however, are diffusion-controlled at the interface level. In order to distinguish between these two contributions, we plot in Fig. 7(b) the averaged traveling length $\langle l \rangle$ divided by the mean radius of precipitates $\langle R \rangle$ at each time step, which represents the mean distance traveled by precipitates due to conventional ripening (growth/shrinkage). It is found that although natural ripening is slow in the presence of chemomechanical coupling, precipitates relocate significantly as a result of elastic interaction. This phenomenon can be seen comparing the different time steps in Fig. 6. During normal growth and ripening the surviving precipitates approximately keep their initial position while chemomechanical coupling leads to severe relocation of precipitates at a nearly constant precipitate size and number. These movements lead to arrangement of the precipitates in certain crystallographic directions as discussed in the following.

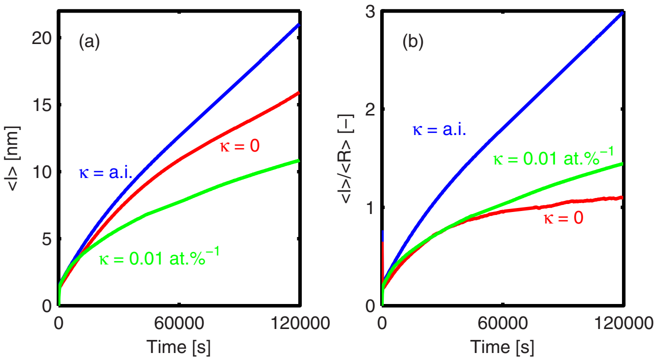

FIG. 7. (a) Average motion of all precipitates and (b) averaged motion rescaled by the average precipitate radius.

The elastic interaction between the precipitates generally exist without the chemomechanical coupling as it is also mentioned in previous works (see, for example, Refs. [73,74]). Under the coupling constraint, however, precipitates last longer and have the chance to interact at a much larger time and length scale. While pressure inside the precipitates slightly increases with the activation of chemomechanical coupling (see Fig. 5) due to an overall increase of the matrix stiffness, the pressure in the matrix forms significant patterns. The interaction of the precipitates follows the elastic properties of the matrix which means that the precipitates align themselves along the softer crystallographic directions as proposed in Refs. [75,76]. Wang *et al.* [63,64] have shown that the precipitates may rearrange due to long-range elastic interactions. 3D microstructures in Fig. 5 also shows the alignment of precipitates. These precipitates show a kidney shape due to strong elastic interaction with one another. This is also observed experimentally, where δ' precipitates were found sitting close to the dislocations [70].

To explore the rearrangement of precipitates and the effect of chemomechanical coupling in a systematic way, we track the angular relation between the neighboring precipitates as described in Sec. III C. The results are presented in Fig. 8. The green lines represents the angles corresponding to either $\langle 0\ 0\ 1 \rangle$ or $\langle 1\ 1\ 1 \rangle$ directions. For Al matrix, the alignment of precipitates is expected along the $\langle 0\ 0\ 1 \rangle$ directions, i.e., the major axis in the cubic coordinate system, due to weak elastic anisotropy of Al and precipitate phase. This corresponds to $\Phi = 0$ and $\theta = 90^\circ$ in our maps. For $\kappa = 0$, the rearrangement of precipitates is confirmed but the statistics are weak due to the fast ripening kinetics (first row in Fig. 8). The simulation results for $\kappa = 0.01$ at.%$^{-1}$ show the same preferred orientations for the alignment. In fact, the isotropic coupling does not influence the elastic response of the matrix but only amplifies its effect because the precipitates persist and interact with one another for a longer period of time. Anisotropic coupling factors ($\kappa =$ a.i.), however, lead to a complete different arrangement of precipitates over the course of ripening. Instead of $\langle 0\,0\,1 \rangle$ orientations, $\langle 1\,1\,1 \rangle$ orientations in the matrix are preferred for the alignment of the precipitates. The last row in Fig. 8 shows the alignment of precipitates close to diagonals. This is in complete agreement with the thought simulation presented in Ref. [29]. The third column (pressure maps) in Fig. 5 displays the aligned precipitates along the $\langle 0\ 0\ 1 \rangle$ (for isotropic coupling) and $\langle 1\ 1\ 1 \rangle$ (for anisotropic coupling) directions. Low-pressure regions around precipitates can be observed in certain directions which are energetically favourable positions for neighboring precipitates. In fact, the negative coupling factor for C_{12} that has been proposed by our DFT calculations leads to a softening along the $\langle 1\ 1\ 1 \rangle$ direction. Note that the magnitude of pressure in Fig. 5 varies for different coupling conditions. The sequence of precipitates rearrangement can be observed in Fig. 6. While the precipitates have the same initial sites (500 s) for different settings, they seek for different energetically favourable patterns with respect to the neighboring precipitates.

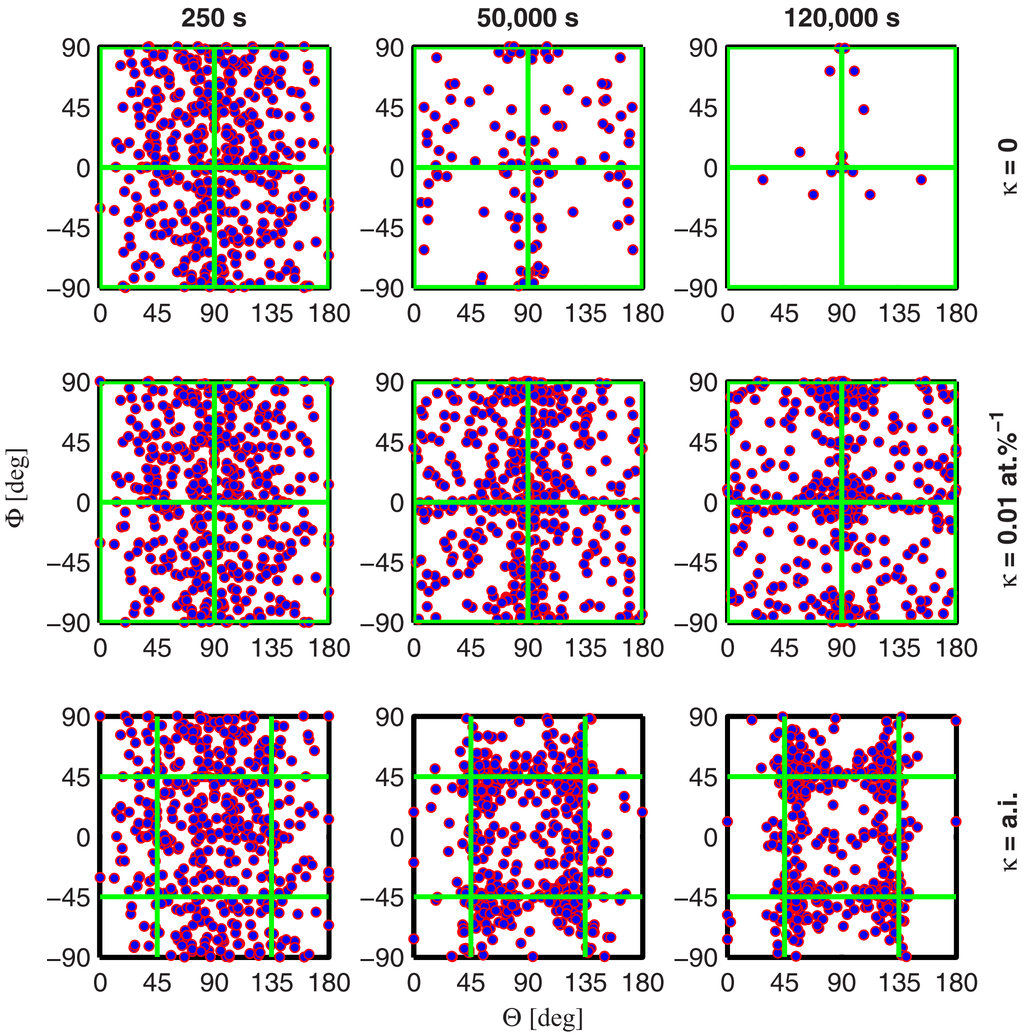

FIG. 8. Orientation of the nearest neighbor (distance <32 nm) in spherical coordinates for different simulation settings after 120 000 s. Green lines show favourable directions of rearrangements: variants of ⟨1 0 0⟩ for no coupling and isotropic coupling and variants of ⟨1 1 0⟩ and ⟨1 1 1⟩ for anisotropic coupling.

C. Remarks on the inverse ripening

The mechanism of inverse ripening [29] suggests that the precipitates shall converge to the same size over the course of ripening. This is in contrast to the conventional ripening where a continuous growth of the average precipitate size is observed. Large-scale simulations also show narrowed size

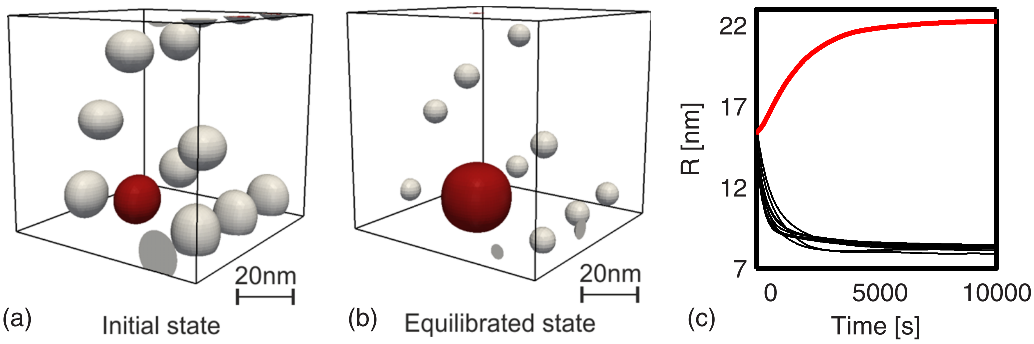

FIG. 9. (a) Microstructure at the initial state (all precipitates have similar size) and (b) at an equilibrated state after a single precipitate (red) lost its coherency (bottom). (c) Individual precipitate radii over time (black lines: coherent precipitates, red line: incoherent precipitate).

distributions of the precipitates depending on the conditions of chemomechanical coupling and positioning of the precipitates [Figs. 3(c) and 3(d)]. In a real microstructure such as observed in the experiments, however, the chemomechanical effect will be greatly influenced by other sources of strains such as dislocations and grain boundaries that disturb self-stress around the precipitates. Hence, the inverse ripening, which strongly depends on the stress fields around precipitates, may not be possible. In order to clarify this fact, we investigate coherency-loss at the matrix/precipitate interface which is a potential disturbance to the mechanical state of the system and its effect on the inverse ripening. In fact, coherency loss is a commonly observed phenomenon in Al alloys where coherent and semicoherent precipitates become incoherent [77]. The loss of coherency is modelled by weakening the shear modulus C_{44} (keeping C_{11} constant) at the interface that mimics the deregistration of the atoms in the precipitate from the corresponding atoms in the matrix. We adjust the coherency-loss of a single precipitate in a multi-precipitate system (ten precipitates) and study the effect of chemomechanical coupling. The results are shown in Fig. 9. It is found that the precipitate with coherency-loss feature [coloured red in Figs. 9(a) and 9(b)] grows at the expense of all other precipitates and a rather conventional process of ripening is recovered [Fig. 9(c)].

Despite being generic for multicomponent solid solutions, the impact of the chemomechanical coupling can be masked by different elements of microstructure evolution. Similar to the coherency-loss, these elements of microstrucutre evolution may result in recovering of the conventional ripening that are to be discussed in the future works. Long-lasting stability of small clustering of precipitates is reported for Al-Cu-Mg alloys [78] that is worth further investigation in the framework of current theory [29]. Heterogeneous nucleation of precipitates on dislocations and grain boundaries are the main sources of disturbance for the self-stress around the precipitates. Thus, in order to capture the features of chemomechanical coupling, precipitation from an undistorted lattice of solid solution and far from the grain boundaries shall be investigated. High-resolution imaging of concentration fields allows to identify strained concentration gradients at the early stages of precipitation. *In situ* investigations of precipitation might be helpful to characterize the rearrangement of small precipitates in a confined volume of bulk.

V. CONCLUSIONS

Large-scale phase-field simulations have been performed under the condition of chemomechanical coupling between the concentration and elastic constants of the matrix phase. We have used DFT calculations to obtain the exact solute composition-dependency of the elastic constants. Inverse ripening and rearrangement of precipitates is observed for randomly initialized precipitates. Our findings demonstrate that the rearrangement and alignment pattern of precipitates strongly depends on the coupling. An anisotropic coupling as obtained for Al-Li system leads to alignment of precipitates along $\langle 1\,1\,1 \rangle$ direction. The chemomechanical coupling feature presented here is generic and present in most multi-component solid solutions subject to stress, but it can be disturbed and superimposed by different elements of microstructure evolution. We have remarked one possible recovering mechanisms of the conventional ripening, i.e., coherency loss, which often occurs in precipitation-hardened alloys.

ACKNOWLEDGMENTS

Financial supports from Deutsche Forschungsgemeinschaft (DFG) under Grants DA 1655/1-1 and HI 1300/8-1 within the priority program SPP-1713 “Strong coupling of thermochemical and thermomechanical states in applied materials” are highly acknowledged. We would like to thank Ingo Steinbach for helpful discussions. In this study, CS conducted phase-field simulations and analysis. AG conducted DFT calculations for solid solutions. TH conceived and supervized DFT calculations. RDK developed the theory of inverse ripening, supervized phase-field investigations, and devised the study.

[1] W. M. Garrison Jr., Ultrahigh-strength steels for aerospace applications, JOM **42**, 20 (1990).

[2] R. Darolia, NiAl alloys for high-temperature structural applications, JOM **43**, 44 (1991).

[3] K. Maruyama, K. Sawada, and J. Koike, Strengthening mechanisms of creep resistant tempered martensitic steel, ISIJ Int. **41**, 641 (2001).

[4] Y. Funakawa, T. Shiozaki, K. Tomita, T. Yamamoto, and E. Maeda, Development of high strength hot-rolled sheet steel consisting of ferrite and nanometer-sized carbides, ISIJ Int. **44**, 1945 (2004).

[5] X. Gao, S. M. Zhu, B. C. Muddle, and J. F. Nie, Precipitation-hardened Mg–Ca–Zn alloys with superior creep resistance, Scr. Mater. **53**, 1321 (2005).

[6] J. Sato, T. Omori, K. Oikawa, I. Ohnuma, R. Kainuma, and K. Ishida, Cobalt-base high-temperature alloys, Science **312**, 90 (2006).

[7] J. Wang, J. Meng, D. Zhang, and D. Tang, Effect of Y for enhanced age hardening response and mechanical properties of Mg–Gd–Y–Zr alloys, Mater. Sci. Eng. A **456**, 78 (2007).

[8] A. Pineau and S. D. Antolovich, High temperature fatigue of nickel-base superalloys - a review with special emphasis on deformation modes and oxidation, Eng. Failure Anal. **16**, 2668 (2009).

[9] J. F. Nie, Precipitation and hardening in magnesium alloys, Metall. Mater. Trans. A **43**, 3891 (2012).

[10] G. B. Burger, A. K. Gupta, P. W. Jeffrey, and D. J. Lloyd, Microstructural control of aluminum sheet used in automotive applications, Mater. Charact. **35**, 23 (1995).

[11] E. A. Starke Jr. and J. T. Staley, Application of modern aluminum alloys to aircraft, Prog. Aeronaut. Sci. **32**, 131 (1996).

[12] W. S. Miller, L. Zhuang, J. Bottema, A. J. Wittebrood, P. De Smet, A. Haszler, and A. Vieregge, Recent development in

aluminium alloys for the automotive industry, Mater. Sci. Eng. A **280**, 37 (2000).

[13] W. D. Lockwood, B. Tomaz, and A. P. Reynolds, Mechanical response of friction stir welded AA2024: experiment and modeling, Mater. Sci. Eng. A **323**, 348 (2002).

[14] S. C. Wang and M. J. Starink, Precipitates and intermetallic phases in precipitation hardening Al–Cu–Mg–(Li) based alloys, Int. Mat. Rev. **50**, 193 (2013).

[15] T. Gladman, Precipitation hardening in metals, Mater. Sci. Technol. **15**, 30 (1999).

[16] N. F. Mott and F. R. N. Nabarro, An attempt to estimate the degree of precipitation hardening, with a simple model, Proc. Phys. Soc. **52**, 86 (1940).

[17] H. Gleiter and E. Hornbogen, Precipitation hardening by coherent particles, Mater. Sci. Engin. **2**, 285 (1968).

[18] A. J. Ardell, Precipitation hardening, Metall. Trans. A **16**, 2131 (1985).

[19] E. Nembach and G. Neite, Precipitation hardening of superalloys by ordered γ'-particles, Prog. Mater. Sci. **29**, 177 (1985).

[20] I. M. Lifshitz and V. V. Slyozov, Kinetics of precipitation from supersaturated solid solutions, J. Phys. Chem. Solids **19**, 35 (1961).

[21] C. Wagner, Theorie der Alterung von Niederschlägen durch Umlösen (Ostwald-Reifung), Zeitschrift für Elektrochemie **65**, 581 (1961).

[22] P. Fratzl, O. Penrose, and J. L. Lebowitz, Modeling of phase separation in alloys with coherent elastic misfit, J. Stat. Phys. **95**, 1429 (1999).

[23] J. D. Eshelby, The continuum theory of lattice defects, Solid State Phys. **3**, 79 (1956).

[24] A. G. Khachaturyan, *Theory of Structural Transformations in Solids* (Courier Corporation, Mineola, New York, 2013).

[25] J. W. Cahn, On spinodal decomposition, Acta Metall. **9**, 795 (1961).

[26] J. W. Cahn, On spinodal decomposition in cubic crystals, Acta Metall. **10**, 179 (1962).

[27] R. D. Kamachali, E. Borukhovich, O. Shchyglo, and I. Steinbach, Solutal gradients in strained equilibrium, Philos. Mag. Lett. **93**, 680 (2013).

[28] R. D. Kamachali, E. Borukhovich, N. Hatcher, and I. Steinbach, DFT-supported phase-field study on the effect of mechanically driven fluxes in Ni_4Ti_3 precipitation, Modell. Simul. Mater. Sci. Eng. **22**, 034003 (2014).

[29] R. D. Kamachali and C. Schwarze, Inverse ripening and rearrangement of precipitates under chemomechanical coupling, Comput. Mater. Sci. **130**, 292 (2017).

[30] I. Steinbach and M. Apel, Multi phase field model for solid state transformation with elastic strain, Physica D **217**, 153 (2006).

[31] I. Steinbach, Phase-field models in materials science, Modell. Simul. Mater. Sci. Eng. **17**, 073001 (2009).

[32] R. D. Kamachali and I. Steinbach, 3-D phase-field simulation of grain growth: topological analysis versus mean-field approximations, Acta Mater. **60**, 2719 (2012).

[33] R. D. Kamachali, A. Abbondandolo, K. F. Siburg, and I. Steinbach, Geometrical grounds of mean field solutions for normal grain growth, Acta Mater. **90**, 252 (2015).

[34] R. D. Kamachali, J. Hua, I. Steinbach, and A. Hartmaier, Multiscale simulations on the grain growth process in nanostructured materials, Int. J. Mat. Res. **101**, 1332 (2010).

[35] C. Schwarze, R. D. Kamachali, and I. Steinbach, Phase-field study of Zener drag and pinning of cylindrical particles in polycrystalline materials, Acta Mater. **106**, 59 (2016).

[36] R. D. Kamachali, S. J. Kim, and I. Steinbach, Texture evolution in deformed AZ31 magnesium sheets: Experiments and phase-field study, Comput. Mater. Sci. **104**, 193 (2015).

[37] I. Häusler, C. Schwarze, M. U. Bilal, D. V. Ramirez, W. Hetaba, R. D. Kamachali, and B. Skrotzki, Precipitation of T1 and θ' phase in Al-4Cu-1Li-0.25Mn during age hardening: Microstructural investigation and phase-field simulation, Materials **10**, 117 (2017).

[38] R. Darvishi Kamachali, Grain boundary motion in polycrystalline materials, Ph.D. thesis, Ruhr-University Bochum, Bochum, Germany, 2013.

[39] F. C. Larché and J. W. Cahn, The interactions of composition and stress in crystalline solids, Acta Metall. **33**, 331 (1985).

[40] S.-W. Chen, C.-H. Jan, J.-C. Lin, and Y. A. Chang, Phase equilibria of the Al–Li binary system, Metall. Trans. A **20**, 2247 (1989).

[41] R. Hultgren, P. D. Desai, D. T. Hawkins, M. Gleiser, and K. K. Kelley, Selected values of the thermodynamic properties of binary alloys, Tech. rep., DTIC Document, http://oai.dtic.mil/oai/oai?verb=getRecord&metadataPrefix=html&identifier=ADD095435.

[42] M. Friak, T. Hickel, F. Körmann, A. Udyansky, A. Dick, J. von Pezold, D. Ma, O. Kim, W. A. Counts, M. Šob *et al.*, Determining the elasticity of materials employing quantum-mechanical approaches: From the electronic ground state to the limits of materials stability, Steel Res. Int. **82**, 86 (2011).

[43] D. Psiachos, T. Hammerschmidt, and R. Drautz, *Ab initio* study of the modification of elastic properties of α-iron by hydrostatic strain and by hydrogen interstitials, Acta Mater. **59**, 4255 (2011).

[44] F. D. Murnaghan, The compressibility of media under extreme pressures, Proc. Natl. Acad. Sci. U.S.A. **30**, 244 (1944).

[45] www.openphase.de.

[46] W. D. Callister, *Materials Science and Engineering* (Wiley, New York, 1985).

[47] S. F. Baumann and D. B. Williams, A new method for the determination of the precipitate-matrix interfacial energy, Scr. Metall. **18**, 611 (1984).

[48] N. E. Prasad, A. A. Gokhale, and R. J. H. Wanhill, *Aluminum-lithium Alloys, Processing, Properties, and Applications* (Elsevier, Oxford, UK, 2013).

[49] M. J. Mehl, Pressure dependence of the elastic moduli in aluminum-rich Al–Li compounds, Phys. Rev. B **47**, 2493 (1993).

[50] A. Taga, L. Vitos, B. Johansson, and G. Grimvall, *Ab initio* calculation of the elastic properties of $Al_{1-x}Li_x$ ($x \leqslant 0.2$) random alloys, Phys. Rev. B **71**, 014201 (2005).

[51] G. Kresse and J. Hafner, *Ab initio* molecular dynamics for liquid metals, Phys. Rev. B **47**, 558 (1993).

[52] G. Kresse and J. Furthmüller, Efficient iterative schemes for *ab initio* total-energy calculations using a plane-wave basis set, Phys. Rev. B **54**, 11169 (1996).

[53] J. P. Perdew, K. Burke, and M. Ernzerhof, Generalized Gradient Approximation Made Simple, Phys. Rev. Lett. **77**, 3865 (1996).

[54] S. Boeck, C. Freysoldt, A. Dick, L. Ismer, and J. Neugebauer, The object-oriented DFT program library s/phi/nx, Comput. Phys. Commun. **182**, 543 (2011).

[55] H. J. Monkhorst and J. D. Pack, Special points for Brillouin-zone integrations, Phys. Rev. B **13**, 5188 (1976).

[56] M. Methfessel and A. T. Paxton, High-precision sampling for Brillouin-zone integration in metals, Phys. Rev. B **40**, 3616 (1989).

[57] W. Müller, E. Bubeck, and V. Gerold, in *Aluminium-Lithium Alloys*, edited by C. Baker *et al.* (London Institute of Metals, London, 1986), Vol. III, p. 435.

[58] M. Sluiter, D. De Fontaine, X.-Q. Guo, R. Podloucky, and A. J. Freeman, First-principles calculation of phase equilibria in the aluminum lithium system, Phys. Rev. B **42**, 10460 (1990).

[59] X.-Q. Guo, R. Podloucky, and A. J. Freeman, Structural and electronic structural properties of ordered LiAl compounds, Phys. Rev. B **40**, 2793 (1989).

[60] X.-Q. Guo, R. Podloucky, and A. J. Freeman, First principles calculation of the elastic constants of intermetallic compounds: metastable Al_3Li, J. Mater. Res. **6**, 324 (1991).

[61] T. Uesugi, Y. Takigawa, and K. Higashi, Elastic constants of AlLi from first principles, Mater. Trans. **46**, 1117 (2005).

[62] C. Kittel, *Introduction to Solid State* (Wiley, New York, 1966).

[63] Y. Wang, L.-Q. Chen, and A. G. Khachaturyan, Particle translational motion and reverse coarsening phenomena in multiparticle systems induced by a long-range elastic interaction, Phys. Rev. B **46**, 11194 (1992).

[64] Y. Wang, L.-Q. Chen, and A. G. Khachaturyan, Kinetics of strain-induced morphological transformation in cubic alloys with a miscibility gap, Acta Metall. Mater. **41**, 279 (1993).

[65] C. H. Su and P. W. Voorhees, The dynamics of precipitate evolution in elastically stressed solids–I. inverse coarsening, Acta Mater. **44**, 1987 (1996).

[66] W. C. Johnson, On the elastic stabilization of precipitates against coarsening under applied load, Acta Metall. **32**, 465 (1984).

[67] W. C. Johnson, P. W. Voorhees, and D. E. Zupon, The effects of elastic stress on the kinetics of Ostwald ripening: the two-particle problem, Metall. Trans. A **20**, 1175 (1989).

[68] A. Onuki and H. Nishimori, Pattern formation in phase-separating alloys with cubic symmetry, Phys. Rev. B **42**, 980 (1990).

[69] A. Onuki and H. Nishimori, On Eshelby's elastic interaction in two-phase solids, J. Phys. Soc. Jpn. **60**, 1 (1991).

[70] D. B. Williams and J. W. Edington, The precipitation of δ' (Al3Li) in dilute aluminium-lithium alloys, Metal Science **9**, 529 (1975).

[71] K. Mahalingam, B. P. Gu, G. L. Liedl, and T. H. Sanders, Coarsening of δ' (Al3Li) precipitates in binary Al–Li alloys, Acta Metall. **35**, 483 (1987).

[72] B. A. Pletcher, K. G. Wang, and M. E. Glicksman, Experimental, computational and theoretical studies of δ' phase coarsening in Al-Li alloys, Acta Mater. **60**, 5803 (2012).

[73] A. J. Ardell and R. B. Nicholson, On the modulated structure of aged Ni–Al alloys: with an appendix on the elastic interaction between inclusions by J. D. Eshelby, Acta Metall. **14**, 1295 (1966).

[74] W. C. Johnson and J. K. Lee, Elastic interaction energy of two spherical precipitates in an anisotropic matrix, Metall. Trans. A **10**, 1141 (1979).

[75] C. H. Su and P. W. Voorhees, The dynamics of precipitate evolution in elastically stressed solids – II. particle alignment, Acta Mater. **44**, 2001 (1996).

[76] V. Vaithyanathan and L.-Q. Chen, Coarsening of ordered intermetallic precipitates with coherency stress, Acta Mater. **50**, 4061 (2002).

[77] J. R. Davis, *Aluminum and Aluminum Alloys* (ASM International, New York, 1993).

[78] A. Deschamps, T. J. Bastow, F. de Geuser, A. J. Hill, and C. R. Hutchinson, In situ evaluation of the microstructure evolution during rapid hardening of an Al–2.5Cu–1.5Mg (wt.%) alloy, Acta Mater. **59**, 2918 (2011).